



HAL
open science

Short lifespans of serpentinization in the rocky core of Enceladus: Implications for hydrogen production

A. Zandanel, L. Truche, Roland Hellmann, Andrey Myagkiy, Gael Choblet, G. Tobie

► To cite this version:

A. Zandanel, L. Truche, Roland Hellmann, Andrey Myagkiy, Gael Choblet, et al.. Short lifespans of serpentinization in the rocky core of Enceladus: Implications for hydrogen production. *Icarus*, 2021, 364, pp.114461. 10.1016/j.icarus.2021.114461 . hal-03389018

HAL Id: hal-03389018

<https://hal.science/hal-03389018>

Submitted on 20 Oct 2021

HAL is a multi-disciplinary open access archive for the deposit and dissemination of scientific research documents, whether they are published or not. The documents may come from teaching and research institutions in France or abroad, or from public or private research centers.

L'archive ouverte pluridisciplinaire **HAL**, est destinée au dépôt et à la diffusion de documents scientifiques de niveau recherche, publiés ou non, émanant des établissements d'enseignement et de recherche français ou étrangers, des laboratoires publics ou privés.

Icarus

Short lifespans of serpentinization in the rocky core of Enceladus: implications for hydrogen production

--Manuscript Draft--

Manuscript Number:	ICARUS-D-20-00414
Article Type:	Research paper
Keywords:	Enceladus; Interiors; Geological processes; Serpentinization; Reactive transport modelling
Abstract:	<p>The discovery of a liquid ocean on Saturn's small moon Enceladus and evidence of modern hydrothermal activity provide an unexpected new environment in which to expand the search for life. However, as with the age of the moons themselves, the age of the liquid ocean and any hydrothermal activity therein remains an area of debate. Based on physical and chemical observations from the Cassini mission we can apply known mineral dissolution rates, estimated water-rock ratios from Enceladus' observed density, and variable water flow rates within the rocky core to constrain duration of active serpentinization, and therefore, the maximum age of the liquid water circulation in the core. On this basis we developed a 1-D reactive transport model to compare the effect of initial olivine percentage, grain size, temperature, and flow rate on timespans of primary olivine alteration in a rocky core the size and density of Enceladus'. In most cases, olivine alteration and precipitation of hydrous secondary minerals results in a water-limited alteration regime. An alteration front that propagates in the direction of water flow then controls the overall rate of olivine alteration. Of the parameters explored, high initial olivine percentages and slow fluid flow rates were the strongest predictors of long serpentinization times, while temperature and grain size had a smaller effect. The annual global H₂ production rate in all model cases ($> 1 \times 10^{12}$ moles yr⁻¹) is several orders of magnitude greater than the minimum H₂ release rate calculated from the observed H₂ in Enceladus' plume (1×10^9 moles yr⁻¹), suggesting that any ongoing active serpentinization processes in the core are likely nearing completion. The longest timescales indicate the potential for olivine alteration and H₂ production for up to ~75 Myr, consistent with weathering rates of terrestrial peridotite massifs. If the H₂ produced from Enceladus is sourced from primary mineral alteration, these results suggest that hydrothermal activity in the core of Enceladus developed only very recently – even as recent as within the past 100 Myr.</p>

Short lifespans of serpentinization in the rocky core of Enceladus: implications for hydrogen production

Elsevier¹

Radarweg 29, Amsterdam

5

A. Zandanel^{a}, L. Truche^a, R. Hellmann^a, Andrey Myagkiy^{a,†}, G. Choblet^b, G. Tobie^b*

*^a ISTERre, UMR 5275, CNRS, Université Grenoble Alpes, 1381 rue de la Piscine, BP53
38041 Grenoble, CEDEX 9, France*

10

*^b Laboratoire de Planétologie et Géodynamique, UMR 6112, CNRS, Université de Nantes, 2
chemin de la Houssinière, 44300 Nantes, France*

[†] Current address : Storengy, 92270 Bois-Colombes, France

15

Abstract

The discovery of a liquid ocean on Saturn's small moon Enceladus and evidence of modern hydrothermal activity provide an unexpected new environment in which to expand the search for life. However, as with the age of the moons themselves, the age of the liquid ocean and any hydrothermal activity therein remains an area of debate.

20 Based on physical and chemical observations from the Cassini mission we can apply known mineral dissolution rates, estimated water-rock ratios from Enceladus' observed density, and variable water flow rates within the rocky core to constrain duration of active serpentinization, and therefore, the maximum age of the liquid water circulation in the core. On this basis we developed a 1-D reactive transport model to compare the

25 effect of initial olivine percentage, grain size, temperature, and flow rate on timespans of primary olivine alteration in a rocky core the size and density of Enceladus'. In most cases, olivine alteration and precipitation of hydrous secondary minerals results in a water-limited alteration regime. An alteration front that propagates in the direction of water flow then controls the overall rate of olivine alteration. Of the parameters

30 explored, high initial olivine percentages and slow fluid flow rates were the strongest predictors of long serpentinization times, while temperature and grain size had a smaller

effect. The annual global H₂ production rate in all model cases ($> 1 \times 10^{12}$ moles yr⁻¹) is several orders of magnitude greater than the minimum H₂ release rate calculated from the observed H₂ in Enceladus' plume (1×10^9 moles yr⁻¹), suggesting that any ongoing
35 active serpentinization processes in the core are likely nearing completion. The longest timescales indicate the potential for olivine alteration and H₂ production for up to ~75 Myr, consistent with weathering rates of terrestrial peridotite massifs. If the H₂ produced from Enceladus is sourced from primary mineral alteration, these results suggest that hydrothermal activity in the core of Enceladus developed only very
40 recently – even as recent as within the past 100 Myr.

Keywords: Enceladus, Interiors, Geological processes, Serpentinization, Reactive transport modelling

1. Introduction

Estimating the origin and evolution of the oceans of Saturn's icy moons is an area of
45 research that has rapidly evolved since the acquisition of new data by the Cassini-Huygens mission (1997-2017). Geophysical observations acquired by the Cassini spacecraft indicate the presence of a liquid ocean on Enceladus beneath its icy outer shell (Beuthe et al., 2016; Čadek et al., 2016, 2019; Collins & Goodman, 2007; Iess et al., 2014; Thomas et al., 2016). Gravity data also indicate that the rocky core of
50 Enceladus has a relatively low density (Beuthe et al., 2016; Čadek et al., 2016; Iess et al., 2014), implying porosity of the order of 20-30% (Choblet et al., 2017). An internal heat source from endogenic activity, likely tidal dissipation in the porous core (Choblet et al., 2017; Liao et al., 2020), is thought to be responsible for anomalously high temperatures and ice shell fracturing at the south pole (Porco et al., 2006; Spencer et al., 2006) collocated with vapor plumes emitting to space (Hansen et al., 2006; Waite et al., 2006). In-situ analyses using Cassini's ion and neutral mass spectrometer (INMS) during close flybys have shown that the vapor plume largely comprises water carrying a number of trace constituents, including organic species and ammonia (Waite et al., 2009, 2017). Salt residues found with water ice in the E-ring of Saturn are thought to
60 be sourced by Enceladus' plumes, further indicating that a liquid ocean currently or

recently existed and interacted with a rocky core (Postberg et al., 2009, 2011). Moreover, the Cassini Cosmic Dust Analyzer (CDA) revealed the presence of nanometer-sized silica particles originating from the E-ring, indicative of active silicate-water interactions inside Enceladus (Hsu et al., 2015; Sekine et al., 2015).
65 Finally, H₂ with relatively high H₂:CH₄ ratios was also measured within the vapor plume, both of which are compatible with inorganic H₂ production during hydration and alteration of ultramafic rocks (Waite et al., 2017).

A long-standing debate concerns the age and duration of Enceladus' endogenic activity: is it a transient phenomenon, or is it long-lived? The duration of activity is
70 mostly determined by the availability of internal heat sources, which is intimately linked to the moon's orbital evolution through tidal friction (e.g. Lainey et al., 2012; Meyer & Wisdom, 2007; Neveu & Rhoden, 2019; K. Zhang & Nimmo, 2009). Early estimates based on approximate dissipation inside Saturn, which controls the rate of orbital expansion, indicated that, at equilibrium, tidal heating could not exceed 1 GW
75 (Meyer & Wisdom, 2007), which represents a power at least 5 times smaller than the total power currently emitted at the South Pole (Spencer et al., 2006). This estimate suggested that the activity on Enceladus may be episodic and relatively short-lived (Běhouňková et al., 2012; O'Neill & Nimmo, 2010). Astrometric data then revealed a faster outward migration for Saturn's moons than initially assumed, indicating
80 subsequently that the dissipation inside Saturn is at least 10 times larger than anticipated. This new estimate of Saturn's dissipation implies that 10-15 GW may be generated inside Enceladus at equilibrium (Lainey et al., 2012, 2017). Even if these new constraints solved the power problem, they have raised new issues regarding the origin and age of the moons. More dissipation in Saturn indeed implies rapid orbital expansion
85 and thus suggests that all inner moons were closer to Saturn and its rings in a relatively recent past (Baillié et al., 2019; Charnoz et al., 2011; Neveu & Rhoden, 2019; Noyelles et al., 2019). The successive formation of Saturn's mid-sized moons (Rhea, Dione, Tethys, Enceladus, and Mimas) from the spreading of initially more massive rings is in line with this constraint (Charnoz et al., 2011; Crida & Charnoz, 2012). The age of
90 Enceladus and neighboring moons is then strongly linked to the age of the rings.

The latest measurements performed by the Cassini spacecraft during the Grand Finale sequence, including mass determination (Iess et al., 2014) and contamination of

the rings by non-ice materials (Z. Zhang et al., 2017), were interpreted to mean that the rings are relatively young. This appears consistent with the analysis of Čuk et al. (2016),
95 who proposed a disruption and re-accretion of the inner moons about 100 My ago in order to explain the orbital configurations of Saturn’s moons. The interpretation of a young age of the rings and late formation of the inner moons are, however, questioned by Crida et al. (2019), who argued that the Cassini data is equally compatible with an old ring system. The fresh ice particle supply provided by Enceladus’ activity might
100 even dilute the ring pollution and thus apparently rejuvenate old rings.

The debate still remains open: recent observations of Titan’s expansion rate (Lainey et al., 2020) finally favor a specific dissipation scenario for the Saturn system termed resonance locking (Fuller et al., 2016). In this conceptual framework, while Saturn’s mid-sized inner moons form successively, their age is essentially unconstrained:
105 Enceladus could be between 500 Myr and 4 Gyr old. Even if the ring and inner moons are old, does it also imply that the activity of Enceladus is old and long-lived? Particle deposit features identified on small irregular moons orbiting in the E-ring suggest that the particle accumulation resulting from particle spread in space by Enceladus did not last more than several tens of million years (Hirata et al., 2014), indicating either very
110 short periods of activity during Enceladus’s history or a relatively recent onset of cryovolcanic activity. If the surface activity is a direct consequence of internal activity, this might suggest a late initiation of hydrothermal activity.

These geophysical constraints, combined with chemical constraints inferred from Cassini’s CDA and INMS data, suggest a novel method of evaluating Enceladus’
115 endogenic activity by estimating the timespan of H₂ generation that can result from hydrothermal water-rock reactions within the core. Hydrothermal alteration of ultramafic rocks containing Fe²⁺-bearing minerals that leads to significant H₂ production is a geologically rapid reaction process. The suite of reactions producing H₂ as a by-product of hydration of mafic and ultramafic minerals are often termed
120 serpentinization, originally referring to reaction of Mg- and Fe-bearing olivine (i.e. forsterite and fayalite) to produce serpentine, brucite and magnetite:



Equation (1)



125 Previous estimates of total H₂ production potential in the core of Enceladus show
that with a pristine rocky core of ultramafic mineralogy, oxidation of all Fe-bearing
minerals would result in up to 2×10^{20} moles H₂ produced (Waite et al., 2017). The
annual minimum release rate of H₂ calculated from its concentration in the vapor
plumes is estimated at $1\text{--}5 \times 10^9$ moles yr⁻¹ (Waite et al., 2017). At this rate, water-rock
130 reactions with only 1% of the mass of the rocky core could produce the observed
amount of H₂ for hundreds of millions of years (Waite et al., 2017). However, efficient
water-rock interaction processes may result in much faster rates of serpentinization
(Malamud & Prialnik, 2013), and thus a shorter lifetime of active H₂ production (Vance
& Melwani Daswani, 2020).

135 Analogous Earth environments where submarine peridotite (ultramafic rock
composed of olivine and pyroxene minerals) weathering takes place offer a range of
time intervals for active serpentinization and complete alteration of primary minerals.
In the alkaline and low-temperature Lost City hydrothermal field (LCHF, located along
the Mid-Atlantic Ridge), the rate of serpentinization is estimated to be between a
140 maximum rate of 5.1×10^{-3} km³ year⁻¹ and a conservative rate of 1.2×10^{-4} km³ year⁻¹
(Früh-Green et al., 2003). Based on these rates, total serpentinization of a peridotite
core the size of that of Enceladus (Table 1) would take between 56 and 240 Myr. In
contrast, experimental dissolution studies of olivine powders (Oelkers, 2001;
Pokrovsky & Schott, 2000b) as well as peridotite rock cores (Malvoisin & Brunet,
145 2014) have yielded chemical alteration rates that are orders of magnitude faster than the
maximum alteration rates estimated for the serpentinization of peridotite massifs in
submarine environments. This discrepancy between field and lab serpentinization rates
is often reconciled by invoking greater water-rock ratios in lab experiments compared
to submarine peridotite massifs (White & Brantley, 2003), which emphasizes the
150 importance of rock porosity and water-rock ratios on weathering rates.

While terrestrial peridotite weathering rates present a convenient point of
comparison, the physical properties of Enceladus' core differ in important ways from
Earth's lithosphere. Specifically, the significantly greater geothermal and geobaric
gradients on Earth preclude the widespread existence of cool, low-pressure, high-
155 porosity mafic rock on multi-kilometer scales. In contrast to the average geothermal
gradient of 25–30 °C km⁻¹ in Earth (Arndt, 2011), Enceladus' core is estimated to have

a temperature gradient of less than $1\text{ }^{\circ}\text{C km}^{-1}$ (Choblet et al., 2017). From the measured
 density of Enceladus, the entire 360-400 km diameter core is thought to be
 unconsolidated, comparable in porosity and water content to a water-saturated sand or
 160 sandstone (20-30% water-filled porosity, Choblet et al. 2017). Continuous fluid
 circulation, which is imposed by tidal forcing, coupled with the high porosity of the
 core suggests that chemical alteration rates may be closer to those determined in
 laboratory experiments, and thus far faster than those estimated for terrestrial submarine
 165 weathering of peridotite. Literature-based alteration rates for a primary H_2 producing
 minerals, variable water flow rates as imposed by heterogenous tidal heating patterns,
 and water-rock ratios expected from core density models may then be used to estimate
 timescales of active hydrogen production from primary mineral alteration occurring
 throughout the rocky core of Enceladus. These timescales can, in turn, be used to place
 age constraints on the endogenic activity of Enceladus.

170 **Table 1 Estimated physical properties of Enceladus' core**

Property	Value
Core porosity	20 % ^a
Core volume (m^3)	2.87×10^{16} ^b
Rock mass in core (kg)	6.26×10^{19} ^b
Initial olivine in rock mass	Sum H_2 producible
100 %:	2.5×10^{20}
60 %:	1.5×10^{20}
20 %:	0.5×10^{20}

^afrom Choblet et al. (2017)

^bfrom Waite et al. (2017)

In order to provide constraints on the timescale of aqueous alteration processes inside
 175 Enceladus' core and hence new age estimates on its activity, we present here a 1-D
 reactive transport model of olivine alteration within an unconsolidated rocky core
 consistent with that of Enceladus and other mid-sized icy satellites that may have
 supported liquid water oceans during their evolution. First, we present the 1-D model

180 structure and the parameter space of both representative and end-member alteration conditions, assuming tidally driven porous convection of interstitial water (Choblet et al., 2017). Second, we present the results showing alteration times **are** controlled by the flow rates of water induced by tidal forcing. Third, we define a range of timespans of active olivine dissolution and H₂ production from our model, and finally compare these results to conditions within the core of Enceladus and other icy moons.

185 **2. 1-D modelling method**

2.1 Hydrodynamics and computational parameters

Olivine dissolution is simulated using a reactive multicomponent 1-D transport model in PHREEQC (V. 3.5.0) (Parkhurst & Appelo, 2013). The model simulates directional alteration of a vertical column of primary minerals (olivine) by a steady
190 influx of water (input solution) from an overlying liquid ocean. Solute concentrations in every cell are solved by an Advection-Reaction-Dispersion equation in PHREEQC that is described in detail by Myagkiy et al. (2017). With this method, concentrations change by advection along concentration gradients or by reaction with solid material. Dispersion in our model is set to zero. Excluding dispersion will result in a sharper
195 reaction front and higher solute concentration peaks; this model then underestimates spreading of the concentration front and slightly overestimates local solute concentrations.

The entire column initially contains a rock phase made up of a primary mineral in contact with an input solution. The chemistry of the input solution is a dilute Na-Cl-
200 HCO₃ seawater solution with 0.8 weight % NH₃ (concentrations of input solution constituents (mmol L⁻¹): [Na] = 122, [Cl] = 78.6, [HCO₃] = 39, [NH₃] = 469, [K] = 0.6, [Si] = 0.011, [Mg] = 0.007, [Al] = 6 × 10⁻⁸, and [Fe] = 6 × 10⁻⁸). This is consistent with a range of ocean compositions predicted by previous models equilibrating a carbonaceous chondrite with water (Zolotov, 2007) as well as with a predicted ocean
205 composition based on analyses of the ice grains from Enceladus' vapor plume (Glein et

al., 2015; Hsu et al., 2015). The rock phase adopted in our models is composed solely of pristine Mg-rich olivine ($\text{Mg}_{1.82}\text{Fe}_{0.17}\text{Al}_{0.007}\text{SiO}_4$). This composition is consistent with measurements of San Carlos olivine and of olivine compositions in chondrites (Buseck & Goldstein, 1969; Komatsu et al., 2001; Oelkers et al., 2018). Aluminum is a known trace constituent of olivine and is therefore included in the olivine composition. Olivine is the sole initial mineral in our calculation of H_2 production times and benefits from extensive dissolution kinetics data. While olivine is one of the primary constituents of chondrites, it is far from the sole mineral thought to make up Enceladus' core. Pyroxenes, native iron, and iron-nickel alloys are all found in chondrites and all contribute to H_2 generation during water-rock interaction (Holm et al., 2015). Olivine dissolution rates are here considered as a proxy for other Mg-Fe silicates, as pyroxene minerals have similar dissolution rates compared to olivine in the high pH range (Bandstra et al., 2008). Native iron and iron-nickel alloys are not included in our initial mineral assemblage because oxidation of native metals and alloys, and therefore H_2 kinetic production rates, is instantaneous compared to dissolution rates of silicates. Inclusion of native metals and alloys in the initial model would then increase the initial amount of H_2 produced but would not be expected to increase the overall duration of H_2 production. In addition, the inclusion of additional primary silicate phases (e.g. quartz, amorphous silica) in the initial rock assemblages may contribute to the silica budget and control secondary mineral formation during alteration (Frost & Beard, 2007). Sensitivity tests that included amorphous silica and quartz in the initial rock assemblage of our models showed that including these minerals had little effect on the secondary mineral paragenesis in the conditions of our model, and no effect on the duration of active H_2 production.

All of our models simulate the geochemical evolution of a 140 km long 1-D column, composed of 3500 cells of 40 m length (Fig. 1). 140 km represents ~80% of the core radius as estimated by geophysical observations of Enceladus (Čadek et al., 2016, 2019; Iess et al., 2014; McKinnon, 2015); an analysis of the impact of the column length on the results is included in the discussion section. Porosity for the 1-D column is set at 20%, consistent with the expected porosity given the density of Enceladus (Choblet et al., 2017) and the compaction regime of a small satellite (Vance et al., 2007). Due to code limitations, porosity remains constant in the column for the model duration. It

240 should be noted that while the available porosity remains constant, the amount of water-filled porosity within the pores is allowed to vary (decrease) due to hydration reactions during transport and therefore the water-rock ratio necessarily varies as well. In real weathering profiles, changes in the volume and density of the rock phase during precipitation of secondary minerals can result in complex processes such as compaction or fracturing (Farough et al., 2016; Lafay et al., 2018; L. Zhang et al., 2019) that are not modelled here.

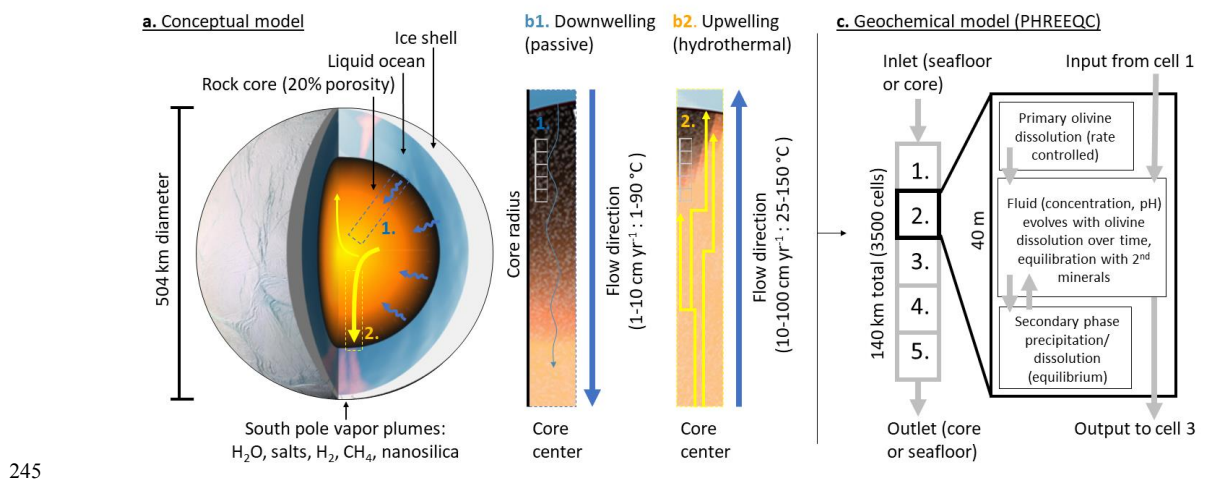


Fig. 1 a. Conceptual model of flow-driven chemical alteration reactions in Enceladus' core (illustration adapted from Choblet et al. 2017): b1) “downwelling” alteration and b2) “upwelling” alteration. c. The PHREEQC geochemical model.

250 A flux boundary condition is imposed on the first cell of the column as fluid input, and on the last cell as fluid output. The flow rate is imposed by selecting the residence time that each batch of fluid interacts with the rock phase (primary olivine + secondary paragenesis) in a single 40 m cell before the fluid is shifted to the next cell in the column (Fig. 1). Each specific flow rate, equal to the residence time divided by the length of the cell (40 m), remains constant during each run (Table 2). The total computing time for 1-D transport calculations is the number of times the solution is shifted vertically through the column. The geologic time represented by each run is determined by multiplying the residence time of the solution in a single cell by the number of times

255

the solution is shifted. Each model runs for an equivalent geologic time of at least 1
 260 Myr, or until all the primary mineral (olivine) in the core is exhausted and the secondary
 paragenesis is at equilibrium with the incoming fluid.

Table 2 Model cases

Case	T (°C)	V (cm yr ⁻¹)	pH (at T)	grain sz (mm)	O:W	<i>t_d</i>	<i>R_{front}</i> km Myr ⁻¹	Flow
1	1	1	11	0.1	4.0:1	35 Myr	3.95	down
2	1	1	11	0.1	2.5:1	22 Myr	6.34	down
3	1	1	11	0.1	1.0:1	300,000 yr	N/A	down
4	1	1	11	1	4.0:1	37 Myr	3.89	down
5	1	1	11	5	4.0:1	58 Myr	3.80*	down
6	25	1	10.7	0.1	4.0:1	35 Myr	4.02	down
7	90	1	10.3	0.1	4.0:1	35 Myr	4.03	up
8	150	1	9.9	0.1	4.0:1	35 Myr	4.03	up
9	150	10	9.9	0.1	4.0:1	4 Myr	40	up
10	150	100	9.9	0.1	4.0:1	380,000 yr	432	up

Temperature (T) and flow rate (V) are constant for each case. pH is of the input solution,
 “grain sz” indicates the radius of the initial olivine grains. O:W is an olivine:water volume
 265 ratio. “Flow” describes whether the V and T are consistent with upwelling fluid or
 downwelling. *t_d* = time until all olivine in the column has been completely dissolved, and
R_{front} = propagation rate of the alteration front (if formed) in km Myr⁻¹.

**R_{front}* for case 5 is calculated for the propagation rate after the formation of an
 alteration front at ~28 Myr.

270

Models use one of three different initial olivine:water (O:W) volume ratios: high
 (4:1), medium (2.5:1) and low (0.8:1). While we do not include additional primary
 minerals, the O:W ratios can be equated to a percent of the rock mass of the core. Given
 an assumed and constant 20 % water-filled porosity, a core of 80 volume % olivine
 275 (equal to 100 volume % of the rock phase) has a 4:1 volume ratio of O:W. In this
 manner, the high, medium, and low initial olivine ratios can be correlated to 80, 50, and
 17 % of the core volume, respectively (or 100, 60, and 20 % of the rock phase by

volume). The O:W ratios were chosen as representative of the range of olivine percentages found in chondrites (Pollack & Chi, 1972). Medium and low O:W ratios are representative of chondrites where a portion of the initial olivine has already undergone aqueous alteration to secondary clay and serpentine minerals (Rubin et al., 2007; Velbel et al., 2012). While the current estimates for a low density core are not consistent with a core composed of 80 % unaltered olivine (Choblet et al., 2017; Waite et al., 2017), the high O:W model is nevertheless included here to represent an end-member scenario of maximum initial olivine. As the amount of H₂ produced is directly proportional to the amount of initial olivine (Eqs. 1 and 2), decreasing the initial olivine percent results in ~~to-~~a decrease in the total amount of H₂ that can be produced (Table 1). The majority of runs use an olivine grain size with 0.1 mm radius, consistent with the average size of olivine chondrules in a collection of carbonaceous chondrites (Rubin, 1989). We also ran cases with olivine grain sizes of 1 mm and 5 mm that simulate larger or more resistant olivine grains (Browning et al., 1996). Specific details of solution pH, O:W ratio, and other model parameters are shown in Table 2.

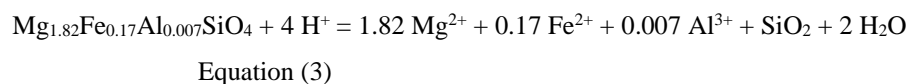
We ran a series of model cases at different temperatures and flow rates (Table 2) consistent with temperatures and flow rates constrained for Enceladus' core by Choblet et al. (2017). In the present study we focus on alteration below 150 °C, where olivine alteration is slower, to illustrate the maximum timescales of olivine dissolution and H₂ production. Computational limitations of the code required that flow rate (water velocity) be held constant over the length of each column for the entire run. Columns were reacted at one of three flow rates: 1, 10, or 100 cm yr⁻¹, corresponding to the range of flow rates obtained by Choblet et al. (2017) for rock permeabilities between 10⁻¹² to 10⁻¹⁵. Temperature was also held constant over time and depth at one of 4 representative values (1, 25, 90, or 150 °C). We assume that water flow completes a circuit from seafloor to core center (downwelling) and from core center to seafloor (upwelling), where the paired temperature and flow rate of each case are relevant either to downwelling (comparatively cold, slow-flow) or upwelling (comparatively hot, fast-flow). As the temperatures of the interior of Enceladus are expected to change over time, some ranges of temperatures and flow rates that may occur in downwelling conditions for periods of the core evolution are consistent with upwelling conditions at

other times. Thus, each 1-D case can represent either a downwelling case or an
310 upwelling case as indicated in Table 2 and illustrated in Fig. 1.

2.2 *Geochemical parameters: rate-controlled olivine dissolution*

Geochemical calculations with PHREEQC used the associated `llnl.dat`
thermodynamic database (Johnson et al., 2000), modified for this study to prevent redox
equilibrium between two separate redox couples: NH_3 - N_2 and CO_2 - CH_4 . Redox
315 equilibrium between dissolved NH_3 and N_2 is kinetically hindered at temperatures at or
below 300°C (Sekine et al., 2015), and the low N_2 measured in Enceladus' plume
(Hansen et al., 2011) suggests NH_3 oxidation is not significant (Waite et al., 2009).
For that reason, the nitrogen-bearing species were decoupled in our database to prevent
thermodynamic equilibration of NH_3 to $\text{N}_2 + \text{H}_2\text{O}$. Similarly, H_2 was decoupled from
320 carbonate species in the database to prevent complete oxidation of CO_2 to CH_4 , which
is incompatible with the elevated $\text{H}_2:\text{CH}_4$ ratio measured in the plume (Waite et al.,
2017).

The rate-controlled dissolution of olivine and the precipitation (or re-dissolution) of
all secondary phases according to their chemical saturation in the fluid are treated as
325 two separate steps in the 1-D model. Olivine dissolution in our model occurs by the
following reaction:



The dissolution process described in Eq. 3 can be considered an elementary reaction
330 of the complex serpentinization reactions described in Eqs. 1 and 2. Rate data for Eq. 3
are readily available in the literature (Bandstra et al., 2008; Oelkers, 2001; Pokrovsky
& Schott, 2000a; Rimstidt et al., 2012). Even though published kinetic data exist for
serpentinization reactions at hydrothermal temperatures (Lamadrid et al., 2017;
Malvoisin et al., 2012; McCollom et al., 2016, 2020), we used olivine dissolution rates
335 rather than serpentinization rates because we are not aware of appropriate rate data for
serpentinization reactions at the much lower temperatures used in our model. Lacking
rate data at low temperatures, precipitation of secondary serpentinite minerals in our

model (chrysotile, brucite, magnetite) is executed instantaneously as a separate step rather than as part of an integrated serpentinization process. Our model does not
340 incorporate potentially competing alteration behaviors such as directly coupled dissolution-serpentinization reactions (Lafay et al., 2012) or kinetic retardation by secondary phases (Daval et al., 2011; Park & Fan, 2004). Instead, olivine dissolution functions as the rate-limiting reaction of serpentinization such as proposed by the experimental studies of Malvoisin et al. (2012) and Okamoto et al. (2011).

345 Aggregated empirical data for San Carlos olivine dissolution suggest that pH and temperature are responsible for up to 90% of the variability in empirically-derived dissolution rates (Rimstidt et al., 2012). The other 10% of variability is influenced by a number of factors, including water activities of < 0.9 . The precipitation of hydrous minerals and the resulting concentration of soluble species in the remaining fluid results
350 in water activities < 0.9 throughout the column in many of the runs. For this reason, we chose to use a specific dissolution rate law for olivine that includes terms for both pH and water activity (Olsen et al., 2015):

$$\log r = [6.05 - 3683 * (1/T)] - 0.52\text{pH} + 3.26 \log a_{\text{H}_2\text{O}}$$

Equation (4)

355 where $\log r$ is the dissolution rate of olivine in $\text{mol m}^{-2} \text{s}^{-1}$ at 25 °C, and the temperature dependence (with T in Kelvin) is calculated as in the general kinetic rate law published in Rimstidt et al. (2012). As PHREEQC requires a non-zero water activity for computation, Eq. 4 also ensures convergence of the numerical method during long alteration timescales where the reactive transport model would otherwise
360 allow the precipitation of hydrous minerals to consume all of the water in the column. No term relating the olivine dissolution rate to the Gibbs free energy of reaction (ΔG) is included in Eq. 4: as less soluble secondary minerals are allowed to precipitate, the fluid-mineral system is always out of equilibrium (undersaturated) with respect to olivine, and therefore the far-from-equilibrium rate of Eq. 4 can be used. The pH term,
365 as integrated in Eq. 4, assumes a linear decrease in the dissolution rate r with increasing pH; however, it is known that this dependence is less pronounced at $\text{pH} > 6$ (McCollom et al., 2020; Wogelius & Walther, 1992). Because of this, the dissolution rate law used in Eq. 4 then calculates slower rates of olivine dissolution than those calculated using

dissolution rate laws resolved over the entire pH range (e.g. Pokrovsky & Schott,
370 2000b; Rimstidt et al., 2012).

The specific olivine dissolution rate expressed by Eq. 4 is embedded in a general
reaction rate formula given by:

$$R_d = r \left(\frac{A_0}{V} \right) \left(\frac{m}{m_0} \right)^n \quad \text{Equation (5)}$$

375 where R_d is the overall reaction rate ($\text{mol L}^{-1} \text{s}^{-1}$), r is the specific dissolution rate
from Eq. 4, A_0 is the initial specific surface area of the olivine ($\text{m}^2 \text{kg}^{-1}$ rock, calculated
geometrically from the selected grain size), V is the volume of solution in contact with
the olivine grains (L kg^{-1} rock); the A_0/V factor approximates the initial olivine surface
area to fluid ratio. m_0 is initial moles of reactant, and m is the moles of reactant at the
380 computational time (Appelo & Postma, 2004). In fact, m represents the moles of
unaltered olivine at time step t , and m_0 is a term that normalizes the moles of olivine at
time step t to a theoretical initial number of olivine moles ($m_0=100$ in all runs). (m/m_0)
can be considered an aging term that serves to decrease the general rate R_d during
dissolution (Appelo & Postma, 2004; Christoffersen, 1976). n is a factor that scales
385 (m/m_0) to simulate the decreases in reactive surface sites (reactive surface area) during
aging, where $n = 0.67$ (or $2/3$) represents a monodisperse grain size population (Dixon
& Hendrix, 1993). As the effect of grain size is explicitly explored as a separate variable
in this study, $n = 0.67$ was used in all models.

The rate expression given by Eq. 5 is employed by PHREEQC at each timestep to
390 calculate olivine dissolution reaction progress. After each kinetically-controlled
reaction step, thermodynamic mineral saturation indices are calculated from the final
fluid composition in each cell. Where selected secondary phases reach chemical
saturation in solution, these minerals are instantaneously precipitated in an amount
proportional to their chemical saturation (or over-saturation). The secondary phases in
395 our model includes those minerals that commonly occur during olivine alteration:
chrysotile (serpentine), amorphous silica, Mg-smectite, brucite, gibbsite, magnesite,
and magnetite. These phases are allowed to precipitate, or even re-dissolve, based on
their thermodynamic stability. Talc was included in the secondary mineral assemblage
at 150°C . We note that although field studies have presented evidence that low-

400 temperature serpentine minerals may form at temperatures of 25 °C or below in
peridotites (Okland et al., 2012; Pfeifer, 1977), there is no consensus as to whether a
minimum temperature for the formation of serpentine minerals exists. Chrysotile is
nevertheless included as a secondary mineral in all models, as the long reaction times
405 support the potential for its formation and sensitivity analyses show that its inclusion
does not affect rates of olivine dissolution nor H₂ production.

Global rates of H₂ production are calculated by normalizing the total moles of H₂
produced in each time step in the entire column to the fixed value of the initial moles
of olivine in the column, giving a rate of H₂ production: mol_{H₂} mol_{initial olivine}⁻¹ year⁻¹.
Annual H₂ production in the column can then be scaled to annual global production by
410 estimating the quantity of moles of olivine initially present in the rocky core from the
imposed O:W volume ratios, the molar volume of olivine, and the inferred volume of
Enceladus' core (Table 1). Limitations of the code prevent exsolution of H₂ from the
fluid during transport, but the complete exsolution of all H₂ produced would almost
certainly not occur instantaneously at the low temperatures in downwelling regions.
415 Moreover, some H₂ would remain dissolved in the fluid and percolate out of the core
by fluid transport. An additional examination of the role of transport through the core
after H₂ production is included in the discussion section.

3. Results and discussion

3.1 *The 1-D transport model: water-limited alteration*

420 The amount of olivine in the 1-D column initially decreases while interacting with
the initial solution in the porous column (Fig. 2). This initial period of elevated water-
rock interaction is analogous to an early phase of water-rock differentiation in small
satellites. During this early phase water ice, initially homogeneously integrated with
other solid phases, melts and migrates through the rock phase to form a liquid reservoir
425 (ocean) differentiated from the rocky core (Malamud & Prialnik, 2016; Schubert et al.,
2007; Vance et al., 2007). During this initial period in our models, olivine dissolution

(Eq. 3) stoichiometrically releases Mg^{2+} , Fe^{2+} , Al^{3+} , and SiO_2 into the fluid at rates dictated by Eq. 5. After this initial period of dissolution, precipitation of secondary minerals causes consumption of the water in each cell (e.g. Eqs. 1 and 2). The decreasing water mass and increasing concentration of solutes in the remaining fluid causes the water activity to decrease from its original value of 1. As olivine dissolution is progressively retarded by decreasing water activity (Eq. 4), the dissolution rate slows during reactive transport until olivine dissolution becomes negligible (2 Myr or less). Without a mechanism to re-introduce water to the core, water-rock interaction would effectively halt after this period of water migration through (and reaction with) the rock core (see e.g. Malamud & Prialnik, 2013, 2016). The incorporation of tidally-driven water circulation through the core provides a mechanism for the reintroduction of water from the overlying liquid ocean: in our model, this is imposed through the fluid input and fluid transport in the column (Fig. 1). An alteration front then forms, where olivine dissolution and secondary precipitation occur only where water is reintroduced to the cells from fluid transport. Ongoing fluid input and transport through the column to the alteration front is what drives its progression in the direction of flow. The time duration for the dissolution of all the olivine in the column (t_d) is then dependent on the rate of propagation of the alteration front (R_{front}), or stated another way, t_d is contingent upon the front passing completely through the column.

The general features of an alteration profile are illustrated in Fig. 2 based on a model run at 25 °C (O:W = 4:1, grain size = 0.1 mm, flow rate = 1 cm yr⁻¹). Fig. 2a shows that any given time, pH in the column increases in the direction of flow as the incoming fluid chemistry is progressively buffered by serpentinization reactions and equilibration with secondary brucite and chrysotile (Leong & Shock, 2020). Fig. 2b shows the moles of H₂ produced in the column as a function of depth. We identified three zones with distinct mineralogy and reactions: an “altered” sector upstream of active alteration, where olivine is completely dissolved (i.e. depleted) and secondary mineralogy is at equilibrium with the incoming fluid; an “alteration front” of active olivine dissolution and hydrous secondary mineral precipitation; and a “water-limited” sector downstream of the front where little olivine dissolution occurs due to low water activity (Fig. 2). The altered sector is dominated by the secondary paragenesis, predominantly chrysotile with small amounts of brucite, magnesite, and magnetite (Fig. 2c-d). pH remains equal

to the pH of the incoming fluid. Within the alteration front, olivine actively dissolves and equilibration of the fluid in each cell at each time step causes Fe^{2+} oxidation to Fe^{3+} , H_2 production, pH increase, and precipitation of chrysotile, magnesite, and brucite (Fig. 2a-c). This is apparent from Fig. 2b, where H_2 production occurs only at the depth of the alteration front: at any given time, less olivine dissolves at the upstream trailing edge of the alteration front where olivine mass is decreased from previous fluid introduction; near the center of the alteration front, more olivine remains and more H_2 is produced; then at the downstream leading edge of the alteration front olivine dissolution and H_2 production decrease again as the increasing pH and decreasing water activity retard the olivine dissolution rate (Eq. 4). We define the leading edge of the alteration front as where olivine dissolution and H_2 production in the downstream edge of the front are near-zero, and the trailing edge as the first cell in the direction of flow to contain a non-zero amount of remaining olivine. In the water-limited sector downstream of the alteration front, olivine remains the principal mineral component with some percent of secondary minerals that precipitated during the initial period of water-rock interaction. The pH in the water-limited zone is higher than that of the incoming seawater (Fig. 2a), having been buffered by the alteration process upstream.

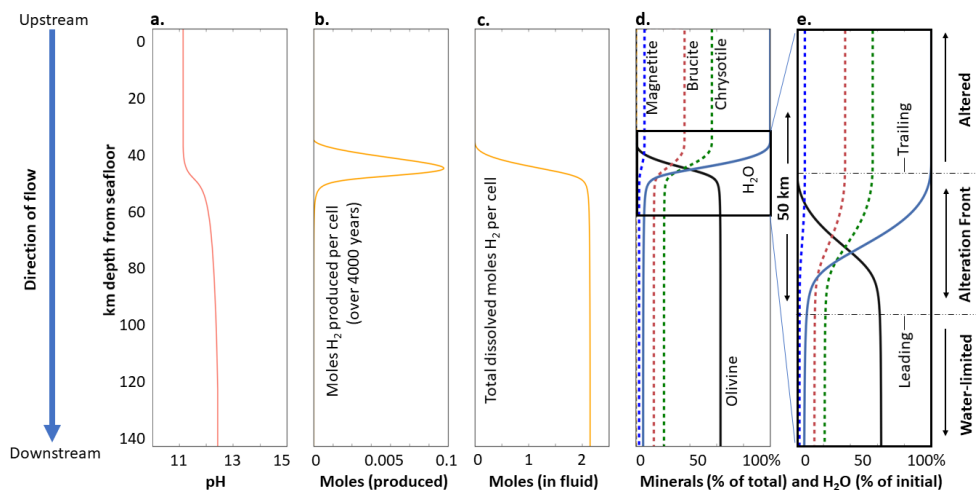


Fig. 2: alteration front at 25 °C, 1 mm grain size, and 1 cm year⁻¹ flow rate after 12 Myr of reaction. a. pH of the fluid in each cell. b. H_2 production in total moles produced per cell in one time step. c. total moles of dissolved H_2 in the fluid phase in each cell: d. Mineralogy

480 regimes in the column: “Minerals (% of total)” is calculated as a percent of the total moles
of all minerals in a given cell, and “H₂O (% of initial)” represents what how much of the 20
% porosity is water-filled. e. Features of the alteration front. The leading and trailing edges
of the alteration front are annotated.

The effect of the various parameters we explored in our models on the shape and the
485 propagation rate of the alteration front through the core is shown in Fig. 3. Increasing
the fluid flow rate has no effect on the shape of the alteration front but causes R_{front} to
increase (Fig. 3a). In Fig. 3b it can be seen that the alteration front changes from a very
sharp step function-like profile with a 5 km width (0.1 mm grain size) to a broad
sigmoidal front with a width of 70 km (5 mm grain size). Grain size also affects the
490 timing and depth of formation of the alteration front: larger grain sizes delay the
formation of an alteration front as the proportionately smaller specific surface area
slows local olivine dissolution rates, allowing water to continue flowing through the
entire column without being completely consumed (Eq. 2). Once the alteration front is
formed, however, changes to grain size have a relatively minor effect on R_{front} (Table
495 2). The initial O:W ratio (Fig. 3c) affects both the formation of an alteration front and
the total olivine dissolution times (t_d). Taking the case with low initial olivine content
(case 3, O:W = 0.8:1, grain size = 0.1 mm, T = 1 °C, flow rate = 1 cm yr⁻¹), all of the
initial olivine in the column is dissolved and converted to secondary minerals during
the initial stage of water-rock interaction. In this case $t_d < 1$ Myr, and is not significantly
500 affected by flow rate because an alteration front never forms. The dependency of the
relative amounts of olivine remaining after the initial water-rock interaction stage on
the initial O:W ratio is shown in Fig. 3c. The final parameter, temperature, alters the
overall shape of the alteration front (Fig. 3d). At 1 °C, the sigmoidal front has a shallow
gradient, extending over several tens of km, while at 150 °C, the front is sharp and
505 resembles a step function.

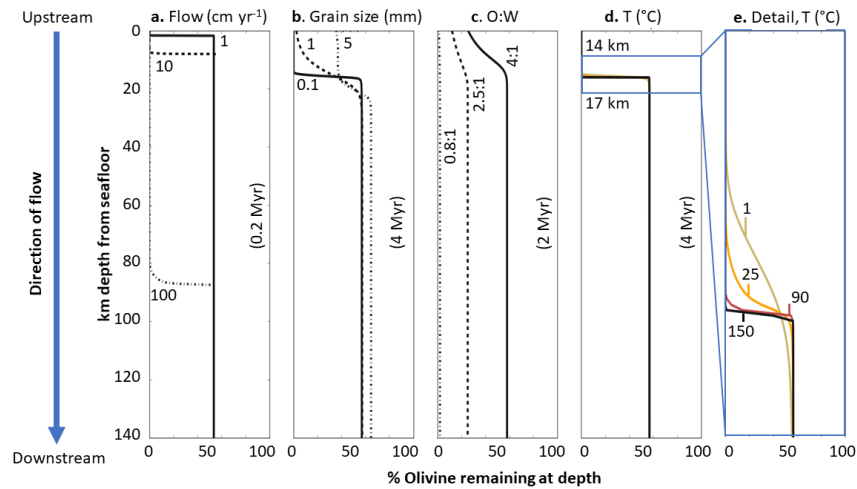


Fig. 3: factors influencing the vertical rate of progress of the alteration front. a. Effect of flow rate (O:W = 4:1, grain size = 0.1 mm, T = 150 °C). b. Effect of grain size (O:W = 4:1, flow rate = 1 cm yr⁻¹, T = 1 °C). c. Effect of the initial O:W (grain size = 0.1 mm, flow rate = 1 cm yr⁻¹, T = 1 °C). d and e. Effect of temperature from 1 to 150 °C (O:W = 4:1, grain size = 0.1 mm, flow rate = 1 cm yr⁻¹).

Once formed, the propagation of the alteration front through the core controls the time required for total alteration of olivine. The dependence of R_{front} on temperature and flow rate is graphically shown in Fig. 4. Figure 4a shows the depth of the alteration front over time, where the depth is defined by the trailing edge of the alteration front (Fig 2e). Six different cases are shown (all starting with O:W ratio = 4:1 and grain size = 0.1 mm): three cases at 150 °C with flow rates of 1, 10, and 100 cm yr⁻¹ to simulate upwelling (Fig 4a); and three additional cases with a 1 cm yr⁻¹ flow rate at temperatures of 1, 25, and 90 °C to simulate downwelling (Fig. 4b). By comparing Figs. 4a and 4b it is apparent that the R_{front} is much more sensitive to flow rate than temperature. By regressing R_{front} (km Myr⁻¹) as a function of flow rate and temperature, the sensitivity of the propagation rate with respect to these two parameters can be quantified (Figs. 4c, d). Figure 4c illustrates that R_{front} scales linearly with flow rate over the range of flow rates explored here. The effect of fluid flow rate on R_{front} (and therefore t_d) is pronounced: increasing the flow rate from 1 cm yr⁻¹ to 10 cm yr⁻¹ decreases t_d from 35

Myr to 4 Myr, which represents a relative decrease of more than 80 % (Fig. 4a). The overall effect of temperature on olivine alteration times is comparatively weak (Fig. 4b): increasing the temperature from 1 to 150°C decreases t_d by less than 5 Myr (< 15 % relative decrease). R_{front} scales logarithmically with respect to temperature (Fig. 4d).

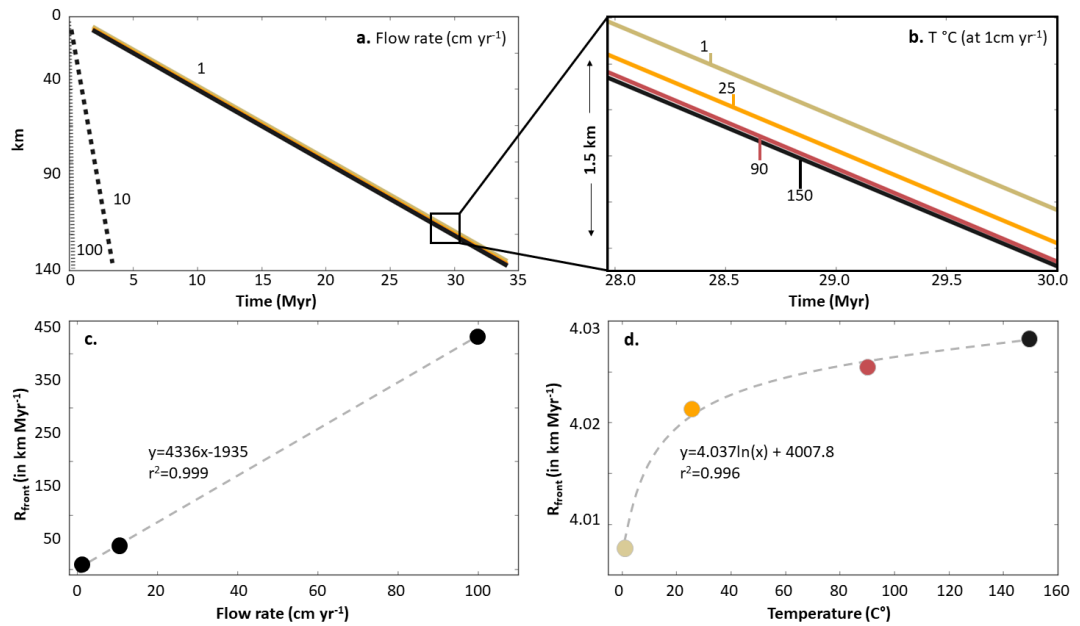


Fig. 4: a. Depth of the alteration front as a function of time, where the depth is defined by the trailing edge of the alteration front ($T = 150\text{ }^{\circ}\text{C}$ for flow rate = 100 and flow rate = 10 cm yr^{-1}). b. inset from a. showing effect of temperature (flow rate = 1 cm yr^{-1}). c. R_{front} regressed over flow rate. d. R_{front} regressed over temperature.

The fixed temperatures and flow rates used here over the entire column length allow us to evaluate the effect of these parameters on the time window of active olivine alteration. In reality, temperature and flow rate are expected to vary with depth and time during Enceladus' evolution (Czechowski & Witek, 2015; Malamud & Prialnik, 2013). In upwelling fluid pathways a thermal gradient from seafloor to core center may vary by up to 10 $^{\circ}\text{C}$, and slower fluid pathways during downwelling may have thermal gradients up to 100 $^{\circ}\text{C}$ (Choblet et al., 2017). Because of this, t_d may be overestimated by model cases that adopt low temperatures and slow water velocities throughout the

545 entire column, and correspondingly underestimated by high-temperature, fast-flow rate
model cases. The longest and shortest windows of active serpentinization in the model
cases are respectively $t_d = 60$ Myr and $t_d = 380,000$ years (Table 2). These windows
can then be considered end-member timescales that would encompass total
serpentinization times of columns that included temperature or water velocity gradients.

550 Considering weathering along a circuit from seafloor to core and back to seafloor
(Fig. 1), the limiting factor in the time needed to totally alter the core will be determined
by the downwelling path due to slower water velocities (Fig. 1 and Table 2). The
existence of upwelling fluids is dependent on there being enough downwelling fluid
remaining, which is then heated in the core to create a hydrothermal upwelling fluid.
555 While there is a high percentage of unaltered olivine remaining, the entire core would
experience downwelling fluid circulation until some minimum water-filled porosity is
established throughout the core. At that point, downwelling through the core and
upwelling through fracture pathways at the poles can occur simultaneously, as
considered in hydrodynamic models of water circulation in the core (Choblet et al.,
560 2017; Liao et al., 2020) and as in the circuit described above. Upwelling paths in any
circuit will then alter faster than their respective downwelling circuits, as they are
subject to higher temperatures and higher water flow rates (Table 2). Therefore, we
consider that the downwelling cases represent the maximum t_d for an entire rocky core
with a radius equal to the column length.

565 3.2 Model limitations

The dependency of t_d on the formation and propagation of an alteration front shows
the importance of considering geochemical reactions over long distances, rather than
applying small-scale models to macroscale processes. In the 140 km column models,
olivine dissolution times were most sensitive to changes in flow rate and initial O:W
570 ratios (Fig. 4). In contrast, the results of sensitivity analyses using a column comprising
only a single 40 m cell (with O:W = 4:1, grain size = 0.1 mm) show that the time
required for total olivine dissolution (t_d) is identical for flow rates at or above 1 cm yr⁻¹
(Fig. 6a). Tests with a 0.1 cm yr⁻¹ flow rate show that the residence time in a single cell

at this flow rate (40,000 years) is long enough that the increased pH and decreased water activity noticeably affect decrease the olivine dissolution rate. Even in this case, however, t_d in the single-cell column is more sensitive to changes in temperature than changes in flow rate. Similarly, in a single cell, t_d is more sensitive to temperature than initial O:W ratio (Fig. 6b). The differences in the results based on the parameters used in a single-cell or batch reactor model, when compared to the importance of the same parameters in the 140 km model, highlights the importance of incorporating reactive transport modeling into interpretations of water-rock interactions in satellites.

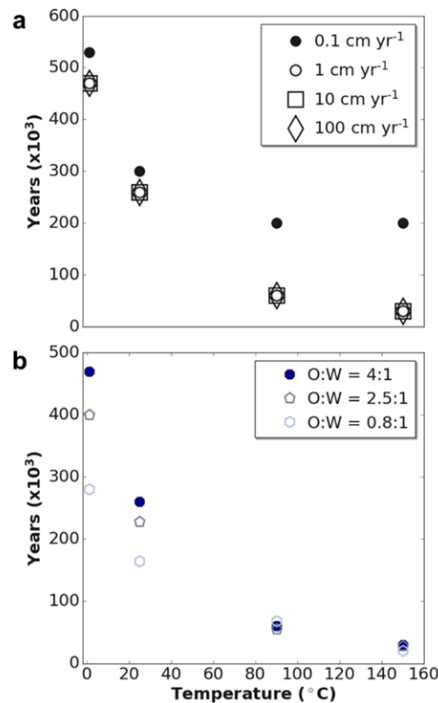


Fig. 6: effect of a. flow rate and b. initial O:W ratio on olivine alteration in a single cell. “Years ($\times 10^3$)” indicates the reaction time necessary to dissolve all olivine in the cell.

585

While modelling geochemical reactions over kilometer-scale distances provides insight into global processes, the use of the 1-D transport model requires necessary simplifications to water-rock interaction processes that would presumably occur in the core. Notably, volume increases of the solid phase during serpentinization are not

590 considered by the code. In our model outputs the total calculated mass of precipitated
secondary minerals would represent a volume increase of more than 30% compared to
the initial olivine. These volume increases have been shown to drive reaction-induced
cracking that can increase serpentinization times in batch reactions by up to an order of
595 magnitude (Malvoisin et al., 2017). Similar reaction-induced fracturing has been
proposed to form a reaction front that can advance at rates of tens of m yr^{-1} in a peridotite
having just 1 % preexisting fracture porosity (Kelemen et al., 2011; Rudge et al., 2010).
Because the porosity of Enceladus' core is up to two orders of magnitude greater than
porosities in terrestrial peridotites (0.8%, Hyndman and Drury 1976) and as the slowest
600 imposed flow rate of 1 cm yr^{-1} in our models is slower than the alteration front
propagation anticipated from reaction-induced cracking, the addition of reaction-
induced cracking to our model would be expected to accelerate R_{front} and increase the
global serpentinization rate.

Another simplification in our model is that olivine dissolution and precipitation of
secondary phases are treated as two separate steps. This ignores any effect of
605 dissolution-precipitation coupling, which has been suggested to decrease long-term
olivine dissolution rates by up to four orders of magnitude in acidic fluids (Daval et al.,
2011). However, in alkaline fluids, this same coupled dissolution-precipitation
mechanism during serpentinization may in fact drive microfracturing at the olivine
surface and promote olivine alteration (Lafay et al., 2018; Plümper et al., 2012). In light
610 of these complexities, general quantitative models of how this factor influences
dissolution rates over time are not readily available. Speculative inhibition of the
dissolution rate over time is approximated by the aging term of Eq. 5, which decreases
the rate by up to two orders of magnitude during runs.

3.3 *Implications for Enceladus' core evolution*

615 Despite the simplifying assumptions inherent to our model, the results are consistent
with timescales of similar processes observed on Earth. The maximum t_d of olivine
alteration in Enceladus' core based on our results would be 35-60 Myr (Table 2). This
range overlaps the estimate of 54-240 Myr for serpentinization of a core the size of

Enceladus' using the peridotite weathering rates proposed by Früh-Green et al. (2003).
620 That our estimates are somewhat shorter is unsurprising given that we assume a porous,
water-saturated core with a mechanism for active water flow within, as opposed to the
low-porosity peridotite massifs that the terrestrial estimates are based from.
Furthermore, our results are comparable to the timescales obtained by Malamud and
Priolnik (2016) for reaching an almost complete core serpentinization during the early
625 evolution of Enceladus. However, for the case of serpentinization that started early on
during Enceladus' history, all olivine should have been exhausted now, and associated
H₂ production by serpentinization should be extremely low. This suggests either that
Enceladus formed very late, and/or that ice melting and hence water circulation have
not developed until recently.

630 A comparison of the time windows of active H₂ production from our 1-D model with
the amount of H₂ currently emitting from Enceladus can be used to estimate the
maximum age of active water-rock interaction. The formation of an alteration front
during reactive transport retards the rate of olivine alteration in the core. This means
that the longest time windows of active olivine serpentinization are in scenarios with
635 delayed alteration front formation and slow alteration front propagation. Olivine
alteration times and corresponding H₂ production for the longest alteration cases (with
O:W = 4:1, T = 1°C, flow rate = 1 cm yr⁻¹) are shown in Fig. 5 for all grain sizes.
Complete alteration of all of the olivine in the core is achieved in 35, 37, and 58 Myr
for grain sizes of 0.1 mm (case 1, Fig. 5a), 1 mm (case 4, Fig. 5b), and 5 mm (case 5,
640 Fig. 5c), respectively. Thus, the slowest end-member case for alteration of the initial
olivine, the window of H₂ production is just under 60 million years. During the entire
58 Myr period, H₂ production is several orders of magnitude larger than the minimum
H₂ release rate calculated from the observed H₂ in the plume (1-5 × 10⁹ moles yr⁻¹, Waite
et al. 2017). During alteration of the initial olivine in the initial stage of water-rock
645 interaction H₂ production rates peak at 3.5 × 10¹³ moles yr⁻¹, and subsequently plateau
at over 2 × 10¹² moles yr⁻¹ as the alteration front propagates through the column (Fig.
5d-f). It is notable that in these models, decreasing the amount of initial olivine must
decrease the total amount of H₂ produced, but it does not affect the rate of H₂
production. For example, case 2 (identical to 1, except for an initial O:W = 2.5:1) also
650 has H₂ production rates that initially peak to > 1 × 10¹³ moles yr⁻¹ and plateau at over 2

$\times 10^{12}$ moles yr^{-1} , but olivine is completely exhausted within 6 Myr (Table 2) The result based on less initial olivine present in the column relative to water-filled porosity, which is analogous to starting with a partially altered rock phase, is that H_2 is produced at the same global annual rate only for a fraction of the time.

655

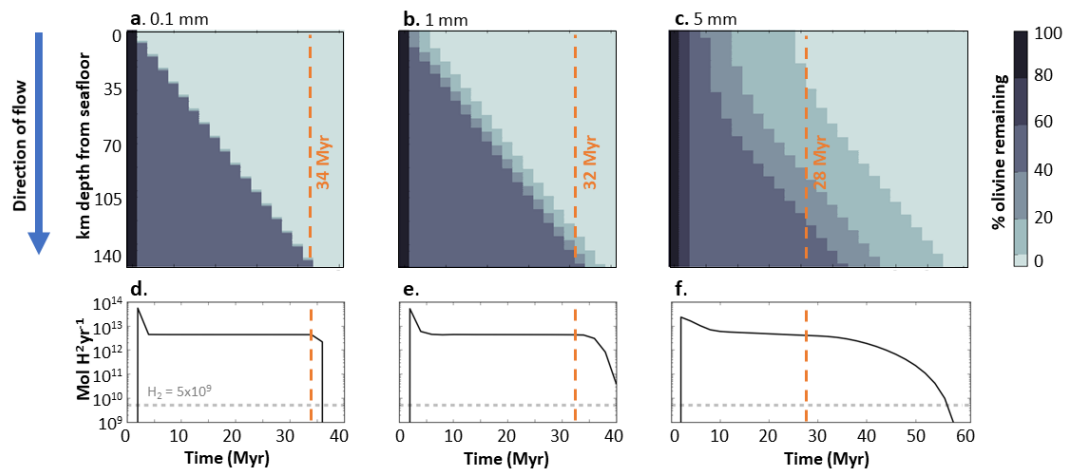


Fig. 5: Depth profiles of olivine dissolution and calculated global H_2 production as a function of time for a. grain size = 0.1 mm. b. grain size = 1 mm and c. grain size = 5 mm. Vertical dashed line indicates the time the leading edge of the alteration front reaches the column terminus. Panels d-f show the global H_2 production over the time corresponding to each of the cases above. Note the initial period of water-rock reaction is reflected in an initial spike in H_2 production. Horizontal dashed line indicates minimum global H_2 release rates from Enceladus.

660

665

To constrain our output to cases that might best reflect current processes in Enceladus, the model output and implications can be compared to the low core density and H_2 emission rates inferred from the data collected by the Cassini mission. We can evaluate the hypothesis that H_2 emitted from Enceladus is evidence of active primary mineral alteration by reviewing model scenarios where H_2 production occurs in a water-saturated column – where the column is not dominated by the water-limited sector as described in Fig. 2. Contemporaneous H_2 production and water-filled porosity over the entire column length can occur in the 1-D reaction transport column in 4 scenarios: 1. imposed flow rates that always exceed the olivine dissolution rate (not modelled here,

670

but as we discuss below, physically not possible); 2. low initial olivine percentage or
675 large grain sizes that prevent the formation of an alteration front (cases 3 and 5,
respectively); 3. in the initial phase of every run where the initial water-filled porosity
interacts with the initial olivine (all cases); 4. during a period of time after an alteration
front progresses through the entire column to intersect the outflow cell (cases 1, 2, 4,
and 6-10). In our models, the 1st scenario requires a flow rate of more than 100,000 cm
680 yr⁻¹, which is not consistent with the physical constraints prescribed by tidal heating
mechanisms (Choblet et al., 2017). Scenarios 2-4 are explored in our models and can
be compared to observations of Enceladus' density and current global H₂ production.

The 2nd scenario is described in our models by either a low initial olivine percentage
available for dissolution or by low olivine specific surface area. A low initial olivine
685 percentage (initial O:W = 0.8:1) completely prevents the formation of an alteration front
even at slow reaction conditions (grain size = 0.1 mm, T = 1°C, flow rate = 1 cm yr⁻¹,
case 3). At such a low O:W ratio, olivine dissolves before the available mass of water
is completely consumed by secondary reactions. This process is relatively rapid and all
of the primary olivine in the core is totally exhausted after 380,000 years of reaction
690 time (Fig. 3d). On the other hand, olivine with low specific surface area delays the
production of an alteration front. At large grain sizes (5 mm, case 5), water flow
continues through the column contemporaneously with olivine dissolution for ~30 Myr
before the formation of an alteration front. However, 5 mm is much larger than the
reported average radius of chondritic olivine chondrules (0.1-0.2 mm, Rubin 1989) and
695 even with moderate grain sizes (1 mm, case 4) an alteration front forms after only 2
Myr of reaction time (Fig. 5c).

The 3rd scenario is a feature of the initial alteration period, analogous to the initial
water-rock interaction period defined by first contact of primary olivine with liquid
water. This initial alteration period is marked by active olivine dissolution as well as
700 water-filled porosity throughout the column. Ultimately, the H₂ production in this
period is markedly high. Vigorous olivine alteration causes global H₂ production rates
to reach values as high as $3\text{-}5 \times 10^{13}$ moles yr⁻¹ before an alteration front forms (Fig. 5d-
f), which is significantly higher than the calculated minimum global H₂ release rate
from Enceladus ($1\text{-}5 \times 10^9$ moles yr⁻¹, Waite et al. 2017). Overall, this period is
705 geologically brief, as the column becomes mostly anhydrous and an alteration front is

formed within 2 Myr. During this transient initial stage, the time span during which the modest rates of observed H₂ release from Enceladus are produced in the column is extremely short-lived in all models, making this scenario rather unlikely.

The 4th scenario corresponds to model cases 1, 2, 4, and 6-10 at the end of the run where the alteration front has progressed through the entire column so that it is near to, or intersecting, the end of the column. The time at which the alteration front reaches the end of the column is indicated in Fig. 5 as an orange dashed line. In the examples shown in Fig. 5 this corresponds to the last several million years of reaction time, where the majority of the column is composed of secondary hydrous minerals and the alteration front has reached the last part of the core (Fig. 5a-c, after ~25 Myr). This scenario is also most consistent with estimated annual H₂ release from Enceladus of 1×10^9 moles yr⁻¹: after the leading edge of the alteration front reaches the end of the column, H₂ production decreases over several Myr from a plateau of 2×10^{12} moles yr⁻¹ to zero after all olivine in the column is dissolved (Fig. 5d-f). The time window between the time where the alteration front first bisects the final cell of the column and t_d is dependent on the shape and the propagation rate of the alteration front. Considering an example case with a very diffuse sigmoidal alteration front and a slow R_{front} (case 5, O:W = 4:1, grain size = 5 mm, T = 1 °C, flow rate = 1 cm yr⁻¹), the alteration front reaches the outflow cell at ~26 Myr and $t_d = 58$ Myr (Fig. 5c). This represents 32 Myr of contemporaneous fluid flow throughout the entire column and active H₂ production. Again, case 5 is an endmember example. Even decreasing the grain radius to 1 mm at the same conditions (case 4, O:W = 4:1, grain radius = 5 mm, T = 1 °C, flow rate = 1 cm yr⁻¹), the time window between the alteration front reaching the outflow cell and t_d decreases to ~6 Myr (Fig. 5b). This time window would be further shortened by increases in the propagation rate or a narrowing of the width of the alteration front (as a result of decreasing the initial O:W ratio, increasing the temperature, or increasing the flow rate).

According to our simulations, in both plausible scenarios (2 and 4) the current low H₂ release production rate from Enceladus thereby implies that olivine alteration in the core is very close to completion, if not already at completion (Fig. 5d-f). As aqueous alteration is very rapid ($t_d < 4$ Myr) in upwelling regions characterized by fast flow and elevated temperature, it is very likely that the olivine in these regions has long since

been altered to secondary phases. The H₂ that we measure today in the plumes is then more likely to have been generated in the coldest parts of the rock core during downwelling (Fig. 6). This apparently contrasts with the model of H₂ generation in Enceladus proposed by Glein et al. (2018) and Glein & Waite, (2020) who concluded that the observed H₂ must be largely sourced by rocks at 250-350 °C in the deep core. This conclusion is not necessarily at odds with our results: as discussed for scenario 4 above, our model also suggests that if alteration is still ongoing it is more likely to be generated within the deeper part of the core (Fig. 5 d-f, Fig. 6). In addition, fluid circulation through a core with very low permeability ($<10^{-16}$ m²) may generate temperatures of >200 °C when reaching the core center (Choblet et al., 2017). However, as olivine alteration rates increase with T until 250-310 °C (Lamadrid et al., 2020; Malvoisin et al., 2012; Wegner & Ernst, 1983), t_d in this case would be shorter than predicted by our models. We also note that the model of Glein et al. (2018) assumes that the fluid in the deep core is in redox equilibrium with serpentizing mafic silicates, whereas the fluid nearer the seafloor is in redox equilibrium with secondary carbonate minerals. This is also consistent with our conclusion that seafloor alteration would occur rapidly, and current production is sourced from within an alteration front that has progressed to the inner core with downwelling fluid (Fig. 6)

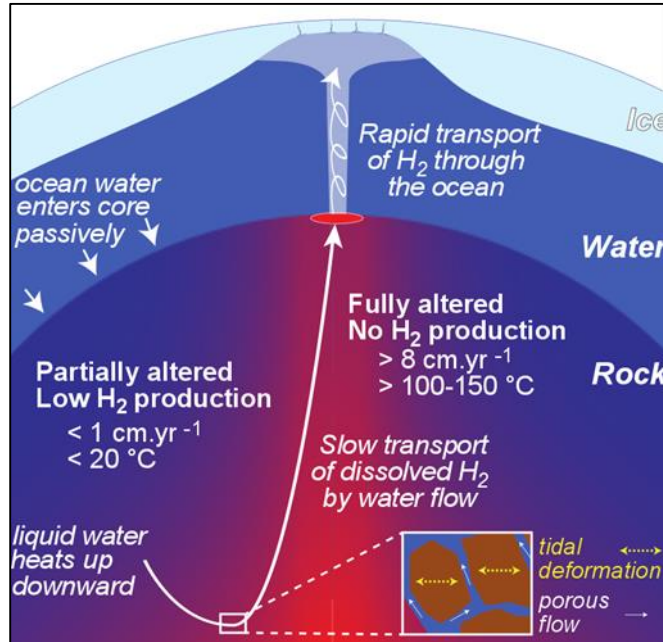


Fig. 6: Conceptual sketch illustrating the fluid flow-driven chemical alteration and the resulting H₂ production and transport in Enceladus' porous core (adapted from Choblet et al. 2017). Most of the present H₂ production is expected to occur during downwelling (flow rate < 1 cm yr⁻¹, T < 20 °C) from the oceanic seafloor to the core center. H₂-rich aqueous fluids progressively heat up in the deep core due to tidal heating, until they become thermally unstable and rise, most notably in the polar regions, in the form of rapid hot water upwelling (flow rate > 8 cm yr⁻¹, T > 100°C). Hot water outflows are responsible for seafloor hotspots triggering oceanic thermal plumes that then transport H₂ rapidly to the jet sources in the ice shell. The whole cycle between the production of H₂ in cold regions and the release at the surface could take several millions of years.

Finally, it might also be possible that primary minerals are totally exhausted at present and that the observed H₂ is being produced by another process or is released over time from a previous production stage. For example, Glein et al. (2018) showed that the production of H₂ by organic pyrolysis can explain the observed H₂ given a high total tidal power within the core (> 50 GW). As for H₂ release over time, the observed high H₂:CH₄ ratios are thought to indicate that long-term H₂ storage is not occurring within Enceladus (Waite et al., 2017). However, the possibility of H₂ release from the

core after active H₂ production has ceased is still possible by a process of flushing H₂-enriched fluids out of the porous core by fluid transport. During downwelling, the H₂ concentration increases in the aqueous fluid as olivine alteration proceeds. Warm aqueous fluids, enriched in H₂, then become unstable and rise preferentially at the poles to feed seafloor hotspots as illustrated in the conceptual model of Fig. 6. According to the simulations of Choblet et al. (2017), the fluid velocity in hot upwellings is estimated between 8 and 80 cm yr⁻¹, for a rock permeability of 10⁻¹⁴-10⁻¹³ m² and a total tidal power between 10 and 30 GW. This would imply transport timescales from the center to the seafloor ranging from 0.2 to 2 Myr. As a consequence, it is possible that the H₂ being ejected into space today was produced a few millions of years ago and is not currently being produced. Considering the typical time for fluid parcels to go through the cold parts of the rock core during downwelling, today's H₂ may even have been produced ~10 Myr ago.

Taken together, these results indicate that the duration of active hydrothermalism on Enceladus, involving production of H₂, is less than 100 Myr. The possibility of several successive hydrothermal episodes throughout the moon's history cannot be ruled out, with active hydrothermal stages whose cumulated duration is a few tens of Myr, interspersed by quiescent periods. The general trend of Saturn's moons' orbital expansion is nevertheless more consistent with a single stage of enhanced production of tidal power, involving the formation of an internal ocean and porous flow in the rocky core. While our results do not provide any constraints on the age of Enceladus, they suggest that the existence of global ocean and the water circulation in the porous core is geologically young, less than 100 Myr old.

3.4 Implications beyond Enceladus' core

The rates of propagation of the alteration front (Table 2) may also be applied to calculate alteration timescales within a longer or shorter column, this being equivalent to changing the radius of the core. For all model cases with a 1 cm yr⁻¹ flow rate (e.g. case 6, O:W = 4:1, grain size = 0.1 mm, T = 25 °C) the alteration front progresses at approximately 4 km yr⁻¹ (Fig. 4c). These alteration rates can then be adapted to the

805 range of estimates for the radius Enceladus core, which vary from 185-190 km (Beuthe
et al., 2016; Čadek et al., 2016; Hemingway et al., 2018). This gives a range of
timescales of active serpentinization of 50-75 Myr given the propagation rates reported
in Table 2. Additionally, we note that these rates could be adapted to estimate the
duration of active serpentinization on other icy satellites where there is evidence of a
810 past or current liquid ocean and an inner rocky core. For example, a column with a
length consistent with the hypothesized rocky core of Saturn's smaller moon Mimas (<
100 km radius, Noyelles et al., 2019) would be totally serpentinized within 25 Myr.
However, for satellites where current observations or models do not adequately
constrain the physical parameters of water flow velocities within a core, these estimates
815 remain speculative.

In icy satellites that do not experience tidally induced water flow throughout a rocky
core, mechanical- or reaction-induced fracturing becomes particularly important.
During alteration, the creation of void space where secondary mineral volume does not
completely replace the water volume lost in hydration reactions may result in
820 potentially irreversible core compaction (Malamud & Prialnik, 2016). This may leave
fracturing as the main driver of introducing water from any liquid ocean to the core,
rather than passive water flow through porous, unconsolidated media. Hydrothermal
models of the dwarf planet Ceres (Neveu et al., 2015) and the Kuiper belt object Orcus
(Malamud & Prialnik, 2015) suggest timescales of fracture propagation over time and
825 maximum depths of fracturing within the rocky cores. The propagation rates described
in these models are on the order of billions of years, timescales at which the reactions
as described in our models would be instantaneous.

4. Conclusions

Using a 1-D reactive transport model, we simulated the serpentinization of
830 Enceladus' core using olivine as an analog mineral. We investigated the effect of initial
olivine percentage, grain size, temperature, and flow rate on the total time needed to
completely alter the primary olivine in a rocky core the size and density of Enceladus'.
In most cases, the alteration of olivine results in precipitation of hydrous secondary

minerals and the formation of an alteration front that slows olivine alteration. For high
835 (4:1) or medium (2.5:1) olivine:water ratios, representative of Enceladus' core, we have
shown that the time of total olivine alteration is controlled by the rate of the vertical
propagation of the alteration front, which separates a completely altered upstream sector
from a water-limited downstream sector with little ongoing alteration. Active olivine
dissolution and precipitation of secondary minerals starts at the leading edge of the
840 alteration front.

Longer serpentinization times are obtained for slower fluid flow rates, lower
temperatures and larger grain sizes. As a consequence, timescales of olivine alteration
in regions characterized by rapid upwelling of hot water ($> 8 \text{ cm yr}^{-1}$, $> 100\text{-}150 \text{ }^\circ\text{C}$)
are geologically very short ($< 500,000 \text{ year}$), while in regions where cold water slowly
845 circulates ($< 1 \text{ cm yr}^{-1}$, $< 20 \text{ }^\circ\text{C}$) timescales can be up to 60 Myr. The latter falls within
the range of expected timespans for alteration of a mass of rock equivalent to
Enceladus' rocky core based on chemical alteration rates of terrestrial peridotite massifs
(Früh-Green et al., 2003).

In all model cases, olivine alteration results in an annual global rate of production of
850 $> 1 \times 10^{12} \text{ moles yr}^{-1}$ for almost the entire lifetime of active H_2 production. This rate is
several orders of magnitude greater than Enceladus' minimum H_2 release rate (1×10^9
 moles yr^{-1}) calculated from the H_2 measured in its vapor plumes (Waite et al., 2017).
This implies that the present release rate corresponds to the tail end of the active H_2
production period with the current H_2 production rate (estimated at $1 \times 10^9 \text{ moles yr}^{-1}$),
855 compatible with exhaustion or quasi-exhaustion of the initial stock of olivine. In our
models such low H_2 production is consistent with cases that either start with a small
initial stock of unaltered olivine in the rock (olivine:water volume ratio $< 0.8:1$, or < 20
vol. % olivine in the rock phase). Alternatively, this low H_2 production may also
correspond to the final stages of the alteration process where the alteration front has
860 progressed through the majority of the column (Figs. 3, 5). The conclusion that
alteration is nearing completion is also consistent with the inferred low density of
Enceladus' core, as olivine is assumed to be replaced by lower-density, hydrous
secondary minerals during alteration. Taken together, these results suggest that the
liquid ocean on Enceladus is geologically young, developing during the last 100 Myr.
865 If the H_2 currently being emitted from Enceladus can be positively attributed to

inorganic production, the results of this study can further serve to constrain the possible length of time that the liquid ocean has existed on Enceladus.

A recent and short-lived duration of hydrothermalism on Enceladus does not reduce the astrobiological interest of this moon. The fact that the hydrothermal activity is recent
870 on Enceladus indeed offer a unique opportunity to study hydrothermal environments during the early stage of planetary evolution. The hydrothermal activity observed today on Enceladus, even if declining, may be representative of various hydrothermal systems that may have active in many other icy bodies. Understanding the chemical complexity emerging in this young hydrothermal system is highly relevant to test the hypothesis
875 that life possibly originated in alkaline hydrothermal vents on Hadean Earth (Martin & Russell, 2007; Russell et al., 2014; Sojo et al., 2016). Even if the geodynamic context on Enceladus is very different from Hadean Earth, Enceladus provides an independent test on the origin of life in hydrothermal environments, which may be addressed by future exploration missions (Choblet & Tobie, 2020). Infra-red mapping of Enceladus'
880 surface revealed that outside the currently active south polar terrain, at least one other region in the northern hemisphere has been recently active (Robidel et al., 2020). This area may be the surface expression of another seafloor hotspot and may preserve chemical signatures of recent hydrothermal activities. Future characterization of the south polar plume activity together with compositional mapping of other recently active
885 centers, such as the one recently identified by Robidel et al. (2020), may provide key insights on how hydrothermal activities involved through time and affected the chemical evolution of Enceladus's ocean.

Acknowledgements

This study acknowledges the financial support from the French Agence
890 Nationale de Recherche, project ANR OASIS (grant N° ANR-16-CE31-0023-01). Laurent Truche acknowledges support from the Institut Universitaire de France. Benjamin Malvoisin is warmly thanked for fruitful discussions over the course of this study.

References

- 895 Appelo, C. A. J., & Postma, D. (2004). *Geochemistry, groundwater and pollution*. CRC
press.
- Arndt, N. (2011). Geothermal Gradient. In M. Gargaud, R. Amils, J. C. Quintanilla, H.
J. (Jim) Cleaves, W. M. Irvine, D. L. Pinti, & M. Viso (Eds.), *Encyclopedia of*
Astrobiology (pp. 662–662). Springer Berlin Heidelberg.
900 https://doi.org/10.1007/978-3-642-11274-4_643
- Baillié, K., Noyelles, B., Lainey, V., Charnoz, S., & Tobie, G. (2019). Formation of the
Cassini Division–I. Shaping the rings by Mimas inward migration. *Monthly*
Notices of the Royal Astronomical Society, 486(2), 2933–2946.
- Bandstra, J. Z., Buss, H. L., Campen, R. K., Liermann, L. J., Moore, J., Hausrath, E.
905 M., Navarre-Sitchler, A. K., Jang, J.-H., & Brantley, S. L. (2008). Compilation
of mineral dissolution rates. *Kinetics of Water-Rock Interaction*, 737–823.
- Běhouňková, M., Tobie, G., Choblet, G., & Čadek, O. (2012). Tidally-induced melting
events as the origin of south-pole activity on Enceladus. *Icarus*, 219(2), 655–
664.
- 910 Beuthe, M., Rivoldini, A., & Trinh, A. (2016). Enceladus's and Dione's floating ice
shells supported by minimum stress isostasy. *Geophysical Research Letters*,
43(19), 10–088.
- Browning, L. B., McSween Jr, H. Y., & Zolensky, M. E. (1996). Correlated alteration
effects in CM carbonaceous chondrites. *Geochimica et Cosmochimica Acta*,
915 60(14), 2621–2633.

- Buseck, P. R., & Goldstein, J. I. (1969). Olivine compositions and cooling rates of pallasitic meteorites. *Geological Society of America Bulletin*, 80(11), 2141–2158.
- Čadek, O., Souček, O., Běhounková, M., Choblet, G., Tobie, G., & Hron, J. (2019). Long-term stability of Enceladus' uneven ice shell. *Icarus*, 319, 476–484.
- Čadek, O., Tobie, G., Van Hoolst, T., Massé, M., Choblet, G., Lefèvre, A., Mitri, G., Baland, R.-M., Běhounková, M., & Bourgeois, O. (2016). Enceladus's internal ocean and ice shell constrained from Cassini gravity, shape, and libration data. *Geophysical Research Letters*, 43(11), 5653–5660.
- Charnoz, S., Crida, A., Castillo-Rogez, J. C., Lainey, V., Dones, L., Karatekin, Ö., Tobie, G., Mathis, S., Le Poncin-Lafitte, C., & Salmon, J. (2011). Accretion of Saturn's mid-sized moons during the viscous spreading of young massive rings: Solving the paradox of silicate-poor rings versus silicate-rich moons. *Icarus*, 216(2), 535–550.
- Choblet, G., & Tobie, G. (2020). Enceladus as a potential oasis for life: Science goals and investigations for future explorations. *Experimental Astronomy*.
- Choblet, G., Tobie, G., Sotin, C., Běhounková, M., Čadek, O., Postberg, F., & Souček, O. (2017). Powering prolonged hydrothermal activity inside Enceladus. *Nature Astronomy*, 1(12), 841.
- Christoffersen, M. R. (1976). The kinetics of dissolution of calcium sulphate dihydrate in water. *Journal of Crystal Growth*, 35(1), 79–88.
- Collins, G. C., & Goodman, J. C. (2007). Enceladus' south polar sea. *Icarus*, 189(1), 72–82.

- 940 Crida, A., & Charnoz, S. (2012). Formation of regular satellites from ancient massive
rings in the solar system. *Science*, 338(6111), 1196–1199.
- Crida, A., Charnoz, S., Hsu, H.-W., & Dones, L. (2019). Are Saturn's rings actually
young? *Nature Astronomy*, 1–4.
- Ćuk, M., Dones, L., & Nesvorný, D. (2016). Dynamical evidence for a late formation
of Saturn's moons. *The Astrophysical Journal*, 820(2), 97.
- 945 Czechowski, L., & Witek, P. (2015). Comparison of early evolutions of Mimas and
Enceladus. *Acta Geophysica*, 63(3), 900–921.
- Daval, D., Sissmann, O., Menguy, N., Saldi, G. D., Guyot, F., Martinez, I., Corvisier,
J., Garcia, B., Machouk, I., & Knauss, K. G. (2011). Influence of amorphous
silica layer formation on the dissolution rate of olivine at 90 C and elevated
950 pCO₂. *Chemical Geology*, 284(1), 193–209.
- Dixon, D. G., & Hendrix, J. L. (1993). Theoretical basis for variable order assumption
in the kinetics of leaching of discrete grains. *AIChE Journal*, 39(5), 904–907.
- Farough, A., Moore, D. E., Lockner, D. A., & Lowell, R. (2016). Evolution of fracture
permeability of ultramafic rocks undergoing serpentinization at hydrothermal
955 conditions: An experimental study. *Geochemistry, Geophysics, Geosystems*,
17(1), 44–55.
- Frost, B. R., & Beard, J. S. (2007). On silica activity and serpentinization. *Journal of
Petrology*, 48(7), 1351–1368.
- Früh-Green, G. L., Kelley, D. S., Bernasconi, S. M., Karson, J. A., Ludwig, K. A.,
960 Butterfield, D. A., Boschi, C., & Proskurowski, G. (2003). 30,000 years of
hydrothermal activity at the Lost City vent field. *Science*, 301(5632), 495–498.

- Fuller, J., Luan, J., & Quataert, E. (2016). Resonance locking as the source of rapid tidal migration in the Jupiter and Saturn moon systems. *Monthly Notices of the Royal Astronomical Society*, 458(4), 3867–3879.
- 965 Glein, C. R., Baross, J. A., & Waite, J. (2015). The pH of Enceladus' ocean. *Geochimica et Cosmochimica Acta*, 162, 202–219.
- Glein, C. R., Postberg, F., & Vance, S. (2018). The geochemistry of Enceladus: Composition and controls. *Enceladus and the Icy Moons of Saturn*, 39.
- Glein, C. R., & Waite, J. (2020). The Carbonate Geochemistry of Enceladus' Ocean.
- 970 *Geophysical Research Letters*, 47(3).
- Hansen, C., Esposito, L., Stewart, A., Colwell, J., Hendrix, A., Pryor, W., Shemansky, D., & West, R. (2006). Enceladus' water vapor plume. *Science*, 311(5766), 1422–1425.
- Hansen, C., Shemansky, D. E., Esposito, L. W., Stewart, A., Lewis, B., Colwell, J.,
- 975 Hendrix, A., West, R. A., Waite Jr, J., & Teolis, B. (2011). The composition and structure of the Enceladus plume. *Geophysical Research Letters*, 38(11).
- Hemingway, D., Iess, L., Tajeddine, R., & Tobie, G. (2018). The interior of Enceladus. *Enceladus and the Icy Moons of Saturn*, 57–77.
- Hirata, N., Miyamoto, H., & Showman, A. P. (2014). Particle deposition on the
- 980 Saturnian satellites from ephemeral cryovolcanism on Enceladus. *Geophysical Research Letters*, 41(12), 4135–4141.
- Holm, N. G., Oze, C., Mousis, O., Waite, J., & Guilbert-Lepoutre, A. (2015). Serpentinization and the formation of H₂ and CH₄ on celestial bodies (planets, moons, comets). *Astrobiology*, 15(7), 587–600.

- 985 Hsu, H.-W., Postberg, F., Sekine, Y., Shibuya, T., Kempf, S., Horányi, M., Juhász, A.,
Altobelli, N., Suzuki, K., & Masaki, Y. (2015). Ongoing hydrothermal
activities within Enceladus. *Nature*, *519*(7542), 207–210.
- Hyndman, R., & Drury, M. (1976). The physical properties of oceanic basement rocks
from deep drilling on the Mid- Atlantic Ridge. *Journal of Geophysical*
990 *Research*, *81*(23), 4042–4052.
- Iess, L., Stevenson, D., Parisi, M., Hemingway, D., Jacobson, R., Lunine, J., Nimmo,
F., Armstrong, J., Asmar, S., & Ducci, M. (2014). The gravity field and interior
structure of Enceladus. *Science*, *344*(6179), 78–80.
- Johnson, J., Anderson, G., & Parkhurst, D. (2000). Database “thermo. Com. V8. R6.
995 230,” Rev. 1-11. *Lawrence Livermore Natl. Lab., Livermore, California*.
- Kelemen, P. B., Matter, J., Streit, E. E., Rudge, J. F., Curry, W. B., & Blusztajn, J.
(2011). Rates and mechanisms of mineral carbonation in peridotite: Natural
processes and recipes for enhanced, in situ CO₂ capture and storage. *Annual*
Review of Earth and Planetary Sciences, *39*, 545–576.
- 1000 Komatsu, M., Krot, A. N., Petaev, M. I., Ulyanov, A. A., Keil, K., & Miyamoto, M.
(2001). Mineralogy and petrography of amoeboid olivine aggregates from the
reduced CV3 chondrites Efremovka, Leoville and Vigarano: Products of
nebular condensation, accretion and annealing. *Meteoritics & Planetary*
Science, *36*(5), 629–641.
- 1005 Lafay, R., Montes-Hernandez, G., Janots, E., Chiriac, R., Findling, N., & Toche, F.
(2012). Mineral replacement rate of olivine by chrysotile and brucite under
high alkaline conditions. *Journal of Crystal Growth*, *347*(1), 62–72.

- Lafay, R., Montes-Hernandez, G., Renard, F., & Vonlanthen, P. (2018). Intracrystalline reaction-induced cracking in olivine evidenced by hydration and carbonation experiments. *Minerals*, 8(9), 412.
- 1010
- Lainey, V., Casajus, L. G., Fuller, J., Zannoni, M., Tortora, P., Cooper, N., Murray, C., Modenini, D., Park, R. S., & Robert, V. (2020). Resonance locking in giant planets indicated by the rapid orbital expansion of Titan. *Nature Astronomy*, 1–6.
- 1015
- Lainey, V., Jacobson, R. A., Tajeddine, R., Cooper, N. J., Murray, C., Robert, V., Tobie, G., Guillot, T., Mathis, S., & Remus, F. (2017). New constraints on Saturn’s interior from Cassini astrometric data. *Icarus*, 281, 286–296.
- Lainey, V., Karatekin, Ö., Desmars, J., Charnoz, S., Arlot, J.-E., Emelyanov, N., Le Poncin-Lafitte, C., Mathis, S., Remus, F., & Tobie, G. (2012). Strong tidal
- 1020
- dissipation in Saturn and constraints on Enceladus’ thermal state from astrometry. *The Astrophysical Journal*, 752(1), 14.
- Lamadrid, H. M., Rimstidt, J. D., Schwarzenbach, E. M., Klein, F., Ulrich, S., Dolocan, A., & Bodnar, R. J. (2017). Effect of water activity on rates of serpentinization of olivine. *Nature Communications*, 8, 16107.
- 1025
- Lamadrid, H. M., Zajacz, Z., Klein, F., & Bodnar, R. (2020). Synthetic fluid inclusions XXIII. Effect of temperature and fluid composition on rates of serpentinization of olivine. *Geochimica et Cosmochimica Acta*, 292, 285–308.
- Leong, J. A. M., & Shock, E. L. (2020). Thermodynamic constraints on the geochemistry of low-temperature, continental, serpentinization-generated
- 1030
- fluids. *American Journal of Science*, 320(3), 185–235.

- Liao, Y., Nimmo, F., & Neufeld, J. A. (2020). Heat production and tidally driven fluid flow in the permeable core of Enceladus. *Journal of Geophysical Research: Planets*.
- 1035 Malamud, U., & Prialnik, D. (2013). Modeling serpentinization: Applied to the early evolution of Enceladus and Mimas. *Icarus*, 225(1), 763–774.
- Malamud, U., & Prialnik, D. (2015). Modeling Kuiper belt objects Charon, Orcus and Salacia by means of a new equation of state for porous icy bodies. *Icarus*, 246, 21–36.
- 1040 Malamud, U., & Prialnik, D. (2016). A 1-D evolutionary model for icy satellites, applied to Enceladus. *Icarus*, 268, 1–11.
- Malvoisin, B., Brantut, N., & Kaczmarek, M.-A. (2017). Control of serpentinisation rate by reaction-induced cracking. *Earth and Planetary Science Letters*, 476, 143–152.
- 1045 Malvoisin, B., & Brunet, F. (2014). Water diffusion-transport in a synthetic dunite: Consequences for oceanic peridotite serpentinization. *Earth and Planetary Science Letters*, 403, 263–272.
- 1050 Malvoisin, B., Brunet, F., Carlut, J., Rouméjon, S., & Cannat, M. (2012). Serpentinization of oceanic peridotites: 2. Kinetics and processes of San Carlos olivine hydrothermal alteration. *Journal of Geophysical Research: Solid Earth*, 117(B4).
- Martin, W., & Russell, M. J. (2007). On the origin of biochemistry at an alkaline hydrothermal vent. *Philosophical Transactions of the Royal Society B: Biological Sciences*, 362(1486), 1887–1926.

- 1055 McCollom, T. M., Klein, F., Robbins, M., Moskowitz, B., Berquó, T. S., Jöns, N., Bach,
W., & Templeton, A. (2016). Temperature trends for reaction rates, hydrogen
generation, and partitioning of iron during experimental serpentinization of
olivine. *Geochimica et Cosmochimica Acta*, *181*, 175–200.
- McCollom, T. M., Klein, F., Solheid, P., & Moskowitz, B. (2020). The effect of pH on
rates of reaction and hydrogen generation during serpentinization.
1060 *Philosophical Transactions of the Royal Society A*, *378*(2165).
- McKinnon, W. B. (2015). Effect of Enceladus's rapid synchronous spin on
interpretation of Cassini gravity. *Geophysical Research Letters*, *42*(7), 2137–
2143.
- Meyer, J., & Wisdom, J. (2007). Tidal heating in Enceladus. *Icarus*, *188*(2), 535–539.
- 1065 Myagkiy, A., Truche, L., Cathelineau, M., & Golfier, F. (2017). Revealing the
conditions of Ni mineralization in the laterite profiles of New Caledonia:
Insights from reactive geochemical transport modelling. *Chemical Geology*,
466, 274–284.
- Neveu, M., Desch, S. J., & Castillo-Rogez, J. C. (2015). Core cracking and
1070 hydrothermal circulation can profoundly affect Ceres' geophysical evolution.
Journal of Geophysical Research: Planets, *120*(2), 123–154.
- Neveu, M., & Rhoden, A. R. (2019). Evolution of Saturn's mid-sized moons. *Nature
Astronomy*, *1*.
- Noyelles, B., Baillié, K., Charnoz, S., Lainey, V., & Tobie, G. (2019). Formation of the
1075 Cassini Division–II. Possible histories of Mimas and Enceladus. *Monthly
Notices of the Royal Astronomical Society*, *486*(2), 2947–2963.

- Oelkers, E. H. (2001). An experimental study of forsterite dissolution rates as a function of temperature and aqueous Mg and Si concentrations. *Chemical Geology*, 175(3–4), 485–494.
- 1080 Oelkers, E. H., Declercq, J., Saldi, G. D., Gislason, S. R., & Schott, J. (2018). Olivine dissolution rates: A critical review. *Chemical Geology*, 500, 1–19.
- Okamoto, A., Ogasawara, Y., Ogawa, Y., & Tsuchiya, N. (2011). Progress of hydration reactions in olivine–H₂O and orthopyroxene–H₂O systems at 250 C and vapor-saturated pressure. *Chemical Geology*, 289(3–4), 245–255.
- 1085 Okland, I., Huang, S., Dahle, H., Thorseth, I., & Pedersen, R. (2012). Low temperature alteration of serpentized ultramafic rock and implications for microbial life. *Chemical Geology*, 318, 75–87.
- Olsen, A. A., Hausrath, E. M., & Rimstidt, J. D. (2015). Forsterite dissolution rates in Mg- sulfate- rich Mars- analog brines and implications of the aqueous
1090 history of Mars. *Journal of Geophysical Research: Planets*, 120(3), 388–400.
- O’Neill, C., & Nimmo, F. (2010). The role of episodic overturn in generating the surface geology and heat flow on Enceladus. *Nature Geoscience*, 3(2), 88–91.
- Park, A.-H. A., & Fan, L.-S. (2004). CO₂ mineral sequestration: Physically activated dissolution of serpentine and pH swing process. *Chemical Engineering
1095 Science*, 59(22–23), 5241–5247.
- Parkhurst, D. L., & Appelo, C. (2013). *Description of input and examples for PHREEQC version 3: A computer program for speciation, batch-reaction, one-dimensional transport, and inverse geochemical calculations* (No. 2328–7055). US Geological Survey.

- 1100 Pfeifer, H. (1977). A model for fluids in metamorphosed ultramafic rocks. - I. Observations at surface and subsurface conditions (high pH spring waters). *Schweizerische Mineralogische Und Petrographische Mitteilungen*, 57, 361–396.
- Plümper, O., Røyne, A., Magrasó, A., & Jamtveit, B. (2012). The interface-scale
1105 mechanism of reaction-induced fracturing during serpentinization. *Geology*, 40(12), 1103–1106.
- Pokrovsky, O. S., & Schott, J. (2000a). Forsterite surface composition in aqueous solutions: A combined potentiometric, electrokinetic, and spectroscopic approach. *Geochimica et Cosmochimica Acta*, 64(19), 3299–3312.
- 1110 Pokrovsky, O. S., & Schott, J. (2000b). Kinetics and mechanism of forsterite dissolution at 25 C and pH from 1 to 12. *Geochimica et Cosmochimica Acta*, 64(19), 3313–3325.
- Pollack, S. S., & Chi, R. D. (1972). Olivine content of chondrites measured by X-ray diffraction. *American Mineralogist: Journal of Earth and Planetary
1115 Materials*, 57(3-4_Part_1), 584–591.
- Porco, C. C., Helfenstein, P., Thomas, P., Ingersoll, A., Wisdom, J., West, R., Neukum, G., Denk, T., Wagner, R., & Roatsch, T. (2006). Cassini observes the active south pole of Enceladus. *Science*, 311(5766), 1393–1401.
- Postberg, F., Kempf, S., Schmidt, J., Brilliantov, N., Beinsen, A., Abel, B., Buck, U.,
1120 & Srama, R. (2009). Sodium salts in E-ring ice grains from an ocean below the surface of Enceladus. *Nature*, 459(7250), 1098–1101.

- Postberg, F., Schmidt, J., Hillier, J., Kempf, S., & Srama, R. (2011). A salt-water reservoir as the source of a compositionally stratified plume on Enceladus. *Nature*, *474*(7353), 620–622.
- 1125 Rimstidt, J. D., Brantley, S. L., & Olsen, A. A. (2012). Systematic review of forsterite dissolution rate data. *Geochimica et Cosmochimica Acta*, *99*, 159–178.
- Robidel, R., Le Mouélic, S., Tobie, G., Massé, M., Seignovert, B., Sotin, C., & Rodriguez, S. (2020). Photometrically-corrected global infrared mosaics of Enceladus: New implications for its spectral diversity and geological activity. *Icarus*, 113848.
- 1130
- Rubin, A. E. (1989). Size- frequency distributions of chondrules in CO3 chondrites. *Meteoritics*, *24*(3), 179–189.
- Rubin, A. E., Trigo-Rodríguez, J. M., Huber, H., & Wasson, J. T. (2007). Progressive aqueous alteration of CM carbonaceous chondrites. *Geochimica et*
- 1135 *Cosmochimica Acta*, *71*(9), 2361–2382.
- Rudge, J. F., Kelemen, P. B., & Spiegelman, M. (2010). A simple model of reaction-induced cracking applied to serpentinization and carbonation of peridotite. *Earth and Planetary Science Letters*, *291*(1–4), 215–227.
- Russell, M. J., Barge, L. M., Bhartia, R., Bocanegra, D., Bracher, P. J., Branscomb, E.,
- 1140 Kidd, R., McGlynn, S., Meier, D. H., Nitschke, W., Shibuya, T., Vance, S. D., White, L., & Kanik, I. (2014). The Drive to Life on Wet and Icy Worlds. *Astrobiology*, *14*(4), 308–343.
- Schubert, G., Anderson, J. D., Travis, B. J., & Palguta, J. (2007). Enceladus: Present internal structure and differentiation by early and long-term radiogenic
- 1145 heating. *Icarus*, *188*(2), 345–355.

- Sekine, Y., Shibuya, T., Postberg, F., Hsu, H.-W., Suzuki, K., Masaki, Y., Kuwatani, T., Mori, M., Hong, P. K., & Yoshizaki, M. (2015). High-temperature water–rock interactions and hydrothermal environments in the chondrite-like core of Enceladus. *Nature Communications*, *6*.
- 1150 Sojo, V., Herschy, B., Whicher, A., Camprubi, E., & Lane, N. (2016). The origin of life in alkaline hydrothermal vents. *Astrobiology*, *16*(2), 181–197.
- Spencer, J., Pearl, J., Segura, M., Flasar, F., Mamoutkine, A., Romani, P., Buratti, B., Hendrix, A., Spilker, L., & Lopes, R. (2006). Cassini encounters Enceladus: Background and the discovery of a south polar hot spot. *Science*, *311*(5766),
- 1155 1401–1405.
- Thomas, P., Tajeddine, R., Tiscareno, M., Burns, J., Joseph, J., Lored, T., Helfenstein, P., & Porco, C. (2016). Enceladus’s measured physical libration requires a global subsurface ocean. *Icarus*, *264*, 37–47.
- Vance, S. D., Kimura, J., DeMartin, B., & Brown, J. M. (2007). Hydrothermal systems
- 1160 in small ocean planets. *Astrobiology*, *7*(6), 987–1005.
- Vance, S. D., & Melwani Daswani, M. (2020). Serpentine and the search for life beyond Earth. *Philosophical Transactions of the Royal Society A*, *378*(2165).
- Velbel, M. A., Tonui, E. K., & Zolensky, M. E. (2012). Replacement of olivine by serpentine in the carbonaceous chondrite Nogoya (CM2). *Geochimica et*
- 1165 *Cosmochimica Acta*, *87*, 117–135.
- Waite, J., Combi, M. R., Ip, W.-H., Cravens, T. E., McNutt, R. L., Kasprzak, W., Yelle, R., Luhmann, J., Niemann, H., & Gell, D. (2006). Cassini ion and neutral mass spectrometer: Enceladus plume composition and structure. *Science*, *311*(5766), 1419–1422.

- 1170 Waite, J., Glein, C. R., Perryman, R. S., Teolis, B. D., Magee, B. A., Miller, G., Grimes,
J., Perry, M. E., Miller, K. E., & Bouquet, A. (2017). Cassini finds molecular
hydrogen in the Enceladus plume: Evidence for hydrothermal processes.
Science, *356*(6334), 155–159.
- Waite, J., Lewis, W., Magee, B., Lunine, J., McKinnon, W., Glein, C. R., Mousis, O.,
1175 Young, D., Brockwell, T., & Westlake, J. (2009). Liquid water on Enceladus
from observations of ammonia and ^{40}Ar in the plume. *Nature*, *460*(7254),
487–490.
- Wegner, W. W., & Ernst, W. (1983). Experimentally determined hydration and
dehydration reaction rates in the system MgO-SiO₂-H₂O. *American Journal*
1180 *of Science*, *283*, 151–180.
- White, A. F., & Brantley, S. L. (2003). The effect of time on the weathering of silicate
minerals: Why do weathering rates differ in the laboratory and field? *Chemical*
Geology, *202*(3–4), 479–506.
- Wogelius, R. A., & Walther, J. V. (1992). Olivine dissolution kinetics at near-surface
1185 conditions. *Chemical Geology*, *97*(1–2), 101–112.
- Zhang, K., & Nimmo, F. (2009). Recent orbital evolution and the internal structures of
Enceladus and Dione. *Icarus*, *204*(2), 597–609.
- Zhang, L., Nasika, C., Donzé, F., Zheng, X., Renard, F., & Scholtès, L. (2019).
Modeling porosity evolution throughout reaction- induced fracturing in rocks
1190 with implications for serpentinization. *Journal of Geophysical Research: Solid*
Earth, *124*(6), 5708–5733.

- Zhang, Z., Hayes, A., Janssen, M., Nicholson, P., Cuzzi, J., de Pater, I., Dunn, D., Estrada, P., & Hedman, M. (2017). Cassini microwave observations provide clues to the origin of Saturn's C ring. *Icarus*, *281*, 297–321.
- 1195 Zolotov, M. Y. (2007). An oceanic composition on early and today's Enceladus. *Geophysical Research Letters*, *34*(23).



[Click here to access/download](#)

Data in Brief

[1D_model_PHREEQC_Zandanel2020.txt](#)

